APL Materials

RESEARCH ARTICLE | OCTOBER 27 2023

Perovskite single crystals with tin–lead gradient for improved ionization radiation detection

Jie Wu ; Xin Wang ; Yubing Xu; Yuzhu Pan; Shunjie Chai; Jingda Zhao; Qi Cheng; Zhiwei Zhao; Qing Li; Byung Seong Bae ; Omolola Esther Fayemi; Jianming Zhou ; Ying Zhu ; Wei Lei

APL Mater. 11, 101130 (2023)
https://doi.org/10.1063/5.0167107

AIP Publishing

APL Materials ARTICLE pubs.aip.org/aip/apm

Perovskite single crystals with tin–lead gradient for improved ionization radiation detection

Cite as: APL Mater. 11, 101130 (2023); doi: 10.1063/5.0167107
Submitted: 10 July 2023 • Accepted: 9 October 2023 •
Published Online: 27 October 2023

Jie Wu,[1] Xin Wang,[1,a)] Yubing Xu,[1] Yuzhu Pan,[1] Shunjie Chai,[1] Jingda Zhao,[1] Qi Cheng,[1] Zhiwei Zhao,[1] Qing Li,[1] Byung Seong Bae,[2] Omolola Esther Fayemi,[3] Jianming Zhou,[4] Ying Zhu,[5] and Wei Lei[1,a)]

AFFILIATIONS

[1] School of Electronic Science and Engineering, Joint International Research Laboratory of Information Display and Visualization, Southeast University, Nanjing 210096, Jiangsu, China
[2] Department of Electronics and Display Engineering Hoseo University, Hoseo Ro 79, Asan City, Chungnam 31499, Republic of Korea
[3] Department of Chemistry, School of Mathematics and Physical Sciences Faculty of Natural and Agricultural Sciences North-West University, Mafikeng Campus, Private Bag X2046, Mmabatho 2735, South Africa
[4] E-spectrum Optoelectronic Co. Ltd., Suzhou 215111, China
[5] E-xray Electronic Co. Ltd., Suzhou 215131, China

[a)] **Authors to whom correspondence should be addressed:** xinw@seu.edu.cn and lw@seu.edu.cn

ABSTRACT

Compared with the pure lead-based $MAPbBr_3$ (MA = CH_3NH_3) perovskite single crystals (PSCs), tin–lead alloy ($MAPb_xSn_{1-x}Br_3$) PSCs with higher carrier mobility and longer carrier lifetime are expected to perform as better-quality ionization radiation detectors. In this work, we design $MAPbBr_3$–$MAPb_{0.9}Sn_{0.1}Br_3$–$MAPb_{0.8}Sn_{0.2}Br_3$ structure detectors by employing solution-process epitaxial growth. Because of the gradient change in tin element proportion, the relatively low mismatch rates between different PSC layers can effectively reduce defects generated at the interface, which improves charge collection efficiency. Moreover, band barriers between different PSC layers form depletion layers due to the differences in band structure, and the high resistivity and built-in electric field of depletion layers can suppress dark current under high voltages. The optimized detector exhibits a high x-ray detection sensitivity of 6.76×10^4 μC Gy^{-1} cm^{-2} and the lowest detectable dose rate of 7.4 nGy s^{-1} under 40 kVp x-ray radiation. Based on ^{241}Am (5.95 MeV) α particle irradiation, tin–lead HD has lower detection noise and more obvious response compared to $MAPbBr_3$ PSCs. The electron mobility was indicated as high as 612 cm^2 s^{-1} V^{-1}, and the mobility-lifetime ($\mu\tau$) products were measured to be 3.5×10^{-3} cm^2 V^{-1} using the Hecht equation, demonstrating superior transport properties.

INTRODUCTION

Ionization radiation detectors are devices that absorb and convert ionization radiation into detectable signals, which have a wide range of applications in industry,[1] medical treatment,[2] security inspection,[3] and other fields. Lead-based perovskite materials [$APbX_3$, where A = MA(CH_3NH_3), HC(NH_2)$_2$, or Cs and X = Br, Cl, or I] have a high average atomic number, strong absorption capacity for high-energy particles, high carrier mobility, low preparation cost, and stable performance, which makes them appealing in the field of ionization radiation detection.[4–6] The x-ray detectors based on printable polycrystalline $MAPbI_3$ thick films can easily be printed on a TFT backplane with benefits at low cost, large area, and low dose.[7] Applying $MAPbI_3$ wafers as active layers to x-ray detectors can achieve a sensitivity up to 1.22×10^5 μC Gy^{-1} cm^{-2}.[34] Although CdZnTe and high-purity Ge (HPGe) semiconductor γ-ray detectors have superior energy resolution, the spread of their applications is still limited due to their high cost and unresolved growth issues.[8,9] Recently, more and more lead-based perovskite materials have shown good γ-ray detection performance.[10,11] All-inorganic perovskite $CsPbBr_3$ devices show a significantly high energy resolution (ER) of 1.4% for 662-keV ^{137}Cs γ-rays,[12] and low temperature solution-grown $MAPbI_3$ PSC achieves 6.8% ER for 122-keV ^{57}Co γ-rays.[35]

However, some unignorable issues still exist in these lead-based perovskites. When detecting high-energy particles, due to the need for a larger thickness of the semiconductor layer, it is necessary to increase bias voltage for improving collection efficiency, which leads to a significant increase in dark current and noise in pure lead-based materials.[14–17] As a result, it is an important task to find ways to explore high-performance detectors of new active materials and complicated structures to suppress dark current and improve signal-to-noise ratio.

Recently, the replacement of Pb by Sn of perovskites is promising according to a series of studies. $APb_mSn_mX_3$ ($0 \leq m \leq 1$) could preserve the original perovskite structure and the most basic photoelectric property.[18–20] Furthermore, compared to pure lead-based perovskites, the bandgap of tin–lead alloy perovskites can be continuously adjusted, and the mobility continues to increase with increasing tin ions.[21,22] These features make tin–lead perovskites widely used in the field of solar cells, but the fabrication of polycrystalline films faces one key challenge: oxidization. The degradation factors of polycrystalline films promote the diffusion of oxygen and water,[23] causing a portion of Sn^{2+} to be oxidized into Sn^{4+}. Therefore, the preparation requires adding extra antioxidants.[24,25] Recently, researchers have found that when the proportion of tin element was below about 40%, the oxidation degree of tin–lead perovskite single crystals (PSCs) was very low compared to polycrystalline films, even without additional oxidation treatment.[23] At the same time, the single crystals have fewer defects and a larger thickness, which leads to a better ability to absorb high-energy particles.

In this work, we report heterojunction detectors based on tin–lead gradient PSCs (tin–lead HDs). We fully utilized the characteristic of adjustable bandgap of tin–lead perovskites to design a kind of P–N heterojunction structure. The depletion layer with high resistivity and built-in electric field formed between different energy bands can effectively suppress dark current. The gradient-proportion design can also reduce lattice mismatch and facilitate the collection of charge carriers. This detector has been tested by x-ray detection and performing alpha spectrum measurements. This work broadens the development field of tin–lead alloy perovskite from polycrystalline films to large-sized single crystals, and these findings also contribute toward detecting x rays and energy-resolved charged particles.

RESULTS AND DISCUSSION

In the fabrication process of detectors based on tin–lead PSCs, high-quality $MAPbBr_3$ PSCs are used as substrates, where $MAPb_{0.9}Sn_{0.1}Br_3$ and $MAPb_{0.8}Sn_{0.2}Br_3$ PSCs were epitaxially grown. Then, the sample was polished and the extra thickness and parts were cut. Finally, gold electrodes are evaporated on the upper and lower surfaces of the sample [Fig. 1(a)]. The photo of the detector ($4.1 \times 5.4 \times 5.4$ mm^3, the thickness of $MAPbBr_3$ substrate: 2.7 mm, $MAPb_{0.9}Sn_{0.1}Br_3$ layer: 1.4 mm, $MAPb_{0.8}Sn_{0.2}Br_3$ layer: 1.3 mm) is shown in Fig. S1. To study the impact of Sn^{2+} doping on the properties of PSCs, we prepared three kinds of PSCs ($MAPbBr_3$, $MAPb_{0.9}Sn_{0.1}Br_3$, and $MAPb_{0.8}Sn_{0.2}Br_3$). As can be appreciated from Table S1, the experimental Pb-to-Sn ratio in the grown single crystal was approximately equal to that in the precursor solution. Therefore, in the following discussion, we directly use the theoretical ratio. The x-ray diffraction (XRD) patterns of these crystals were shown in Fig. 1(b). We found that the positions of the four main diffraction peaks did not shift obviously with the addition of Sn^{2+}. The lattice parameters experienced a clear reduction (from 5.9303 to 5.9221 Å) by increasing the amount of Sn^{2+}, which followed Vegard's law. The mismatch rates,

$$f = \frac{a_1 - a_2}{a_1 + a_2}, \tag{1}$$

(where a_1 and a_2 are the lattice constants of the substrate and epitaxial layer, respectively) are 0.44% for the $MAPbBr_3$–$MAPb_{0.9}Sn_{0.1}Br_3$ junction and 0.25% for the $MAPb_{0.9}Sn_{0.1}Br_3$–$MAPb_{0.8}Sn_{0.2}Br_3$ junction, respectively, which is sufficient enough to realize high-quality epitaxial growth. We obtained the atomic concentration of $MAPb_{0.9}Sn_{0.1}Br_3$ and $MAPb_{0.8}Sn_{0.2}Br_3$ PSCs from XPS measurement (Table S1). The experimentally determined Pb-to-Sn ratios in these grown single crystals were approximately equal to those in the precursor solution. Figure 1(c) illustrates the x-ray photoelectron spectroscopy (XPS) zoom-in spectra for typical Sn peaks in $MAPb_{0.9}Sn_{0.1}Br_3$ and $MAPb_{0.8}Sn_{0.2}Br_3$ PSCs (the whole XPS spectra are shown in Fig. S2). All the two PSCs exhibited only one single characteristic peak of both the $3d_{5/2}$ region and $3d_{3/2}$ region, indicating that only Sn^{2+} existed in the sample. Meanwhile, the spectral feature at a binding energy of 486.4 and 495.2 eV corresponds to Sn^{2+},[26] which also proves that the oxidation of tin–lead PSCs can be almost ignored. From the valence spectra of the $MAPb_{0.9}Sn_{0.1}Br_3$ and $MAPb_{0.8}Sn_{0.2}Br_3$ shown in Fig. 1(d), the energy difference between the valance band maximum (VBM) and Fermi energy (E_F) is 1.44 and 1.23 eV, respectively. Figure 1(e) compares UV–visible absorption spectra for $MAPbBr_3$, $MAPb_{0.9}Sn_{0.1}Br_3$, and $MAPb_{0.8}Sn_{0.2}Br_3$. By increasing the content of Sn^{2+} in PSCs, the absorption from 560 to 650 nm is apparently enhanced. The right small inset picture illustrates the Tauc plot, which demonstrates the decrease i the bandgap from 2.14 to 1.97 eV with the increasing Sn^{2+} substitution. Moreover, due to the low absorption coefficient of Sn,[22] the absorption below ~560 nm clearly declines when Sn^{2+} substitution continues to increase.

The photon-activated charge lifetimes of $MAPbBr_3$, $MAPb_{0.9}Sn_{0.1}Br_3$, and $MAPb_{0.8}Sn_{0.2}Br_3$ were measured by time-resolved photoluminescence (TRPL) [Fig. 1(f)]. The TRPL decay is fitted with a double-exponential decay model, and the fitted lines consist of a fast and a slow component. The fast decay process is caused by the bimolecular recombination of photo-generated free carriers, while the slow decay process is mainly attributed to transfer recombination.[27,28] The average carrier lifetimes τ of $MAPbBr_3$, $MAPb_{0.9}Sn_{0.1}Br_3$, and $MAPb_{0.8}Sn_{0.2}Br_3$ were 6.08, 9.26, and 13.51 μs, respectively, by

$$\tau_{av} = \frac{A_1\tau_1^2 + A_2\tau_2^2}{A_1\tau_1 + A_2\tau_2}. \tag{2}$$

The result indicated that the addition of Sn^{2+} in tin–lead PSCs could reduce the density of traps and inhibit non-radiation recombination. To obtain the mobility of these PSCs, a pulse laser with a 7 ns duration was used, as shown in Fig. 1(g). The result of different drift times of three PSCs confirmed that the higher the tin ion content, the faster the PSC response. In addition, calculation shows that

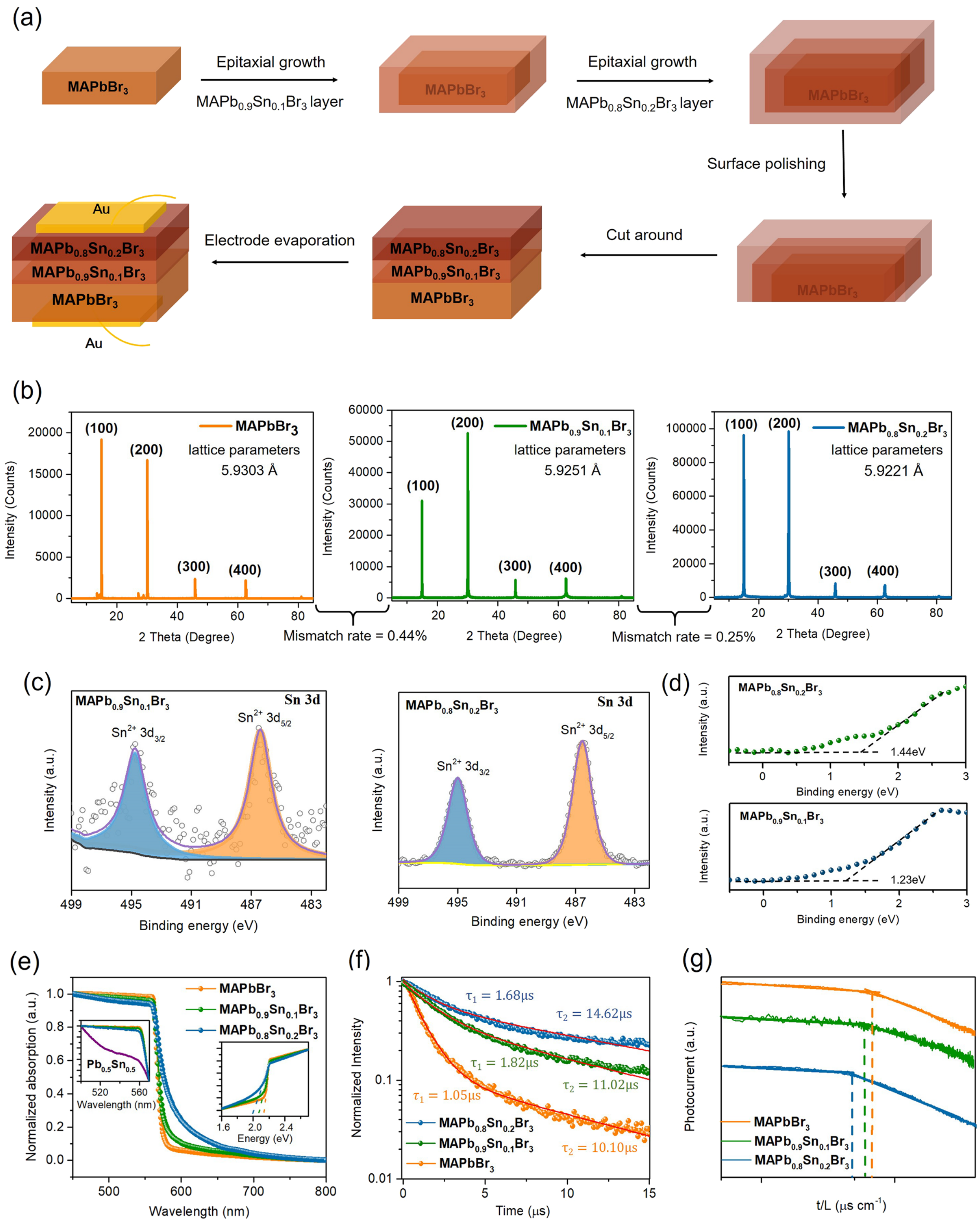

FIG. 1. Three kinds of PSCs' basic properties. (a) Illustration of the fabrication process of the detector. (b) The x-ray diffraction pattern of $MAPbBr_3$, $MAPb_{0.9}Sn_{0.1}Br_3$, and $MAPb_{0.8}$ $Sn_{0.2}Br_3$ PSCs. (c) The x-ray photoelectron spectroscopy (XPS) spectra for Sn 3d of $MAPb_{0.9}Sn_{0.1}Br_3$ and $MAPb_{0.8}$ $Sn_{0.2}Br_3$, respectively. (d) XPS valence spectra of $MAPb_{0.9}Sn_{0.1}Br_3$ and $MAPb_{0.8}Sn_{0.2}Br_3$ (e) Normalized UV–Vis absorption curve of three PSCs. The left inset graph: enlarged local image. The right inset graph: the Tauc-plot. (f) The lifetime of three PSCs is measured by time-resolved photoluminescence. (g) Drift times of three PSCs under the same electric field.

linear absorption cross-section coefficients of $MAPb_{0.9}Sn_{0.1}Br_3$ and $MAPb_{0.8}Sn_{0.2}Br_3$ PSCs do not change obviously and are comparable to the widely used classical CdZnTe semiconductors from a photon energy of 1 keV to 1 MeV (Fig. S3).

The detailed cross section of the $MAPbBr_3$–$MAPb_{0.9}Sn_{0.1}Br_3$–$MAPb_{0.8}Sn_{0.2}Br_3$ structure was investigated by scanning electron microscopy (SEM) [Fig. 2(a)]. Each part of the cross section was flat without the appearance of hole defects and crystal particles, demonstrating the single-crystalline nature of every layer and the high quality of the gradient heterojunction. The conductivity of those bright areas with widths of 7.65 and 6.43 μm near the different two layers was worse than that of their neighboring regions, which are possibly depletion layers.[29] The wider energy bending area leads to a lower capacitance. What is more, we used Kelvin probe force microscopy (KPFM) to measure the depletion layer, as shown in Fig. S4. The electric potential differences of $MAPb_{0.9}Sn_{0.1}Br_3$–$MAPb_{0.8}Sn_{0.2}Br_3$ contact and $MAPb_{0.9}Sn_{0.1}Br_3$–$MAPb_{0.8}Sn_{0.2}Br_3$ contact were ~0.07 and 0.03 eV, and the depletion widths were calculated as 7.8 and 6.2 μm, respectively [Fig. 2(b)]. The tin–lead gradient structure leads to lower barrier potential, which may cause higher electron collection efficiency and a faster speed. Moreover, the width of the depletion layer measured in the KPFM experiments here is in good agreement with the SEM figure. The schematic energy levels of three kinds of PSCs are shown in Fig. 2(c) based on the data of valence spectra from XPS and the figure of the bandgap. The $MAPbBr_3$ is typical P-type, the $MAPb_{0.9}Sn_{0.1}Br_3$ is slightly N-type, and the $MAPb_{0.8}Sn_{0.2}Br_3$ is strongly N-type, which is consistent with the results measured using the Hall Effect.

We characterized the optoelectronic properties of tin–lead HD to further understand the electron transport feature. Figure 3(a) shows the characterization of current density–voltage, indicating that the p–n junction structure formed between tin–lead PSC and pure lead-based PSC. The dark current density was ~0.3 μA cm^{-2} with reverse electrical fields of 150 V cm^{-1}. Compared with $MAPbBr_3$ PSC, the p–n junction structure emerged with lower dark current density by forming potential barriers between different PSC under the applied reverse voltage. The current density increased to nearly 5.3 μA cm^{-2} when illuminated by 520 nm photons with an intensity of 2 mW cm^{-2}. To test the stability of the device, we applied the electric field of −400 V cm^{-1} to the device and observed the changes in dark current [Fig. 3(b)]. When the electric field was first applied, the dark current gradually decreased and finally stabilized at 115 nA after about 1400 s due to the dielectric relaxation, with a fluctuation of no more than 1 nA. The space-charge limited current (SCLC) method is suitable for measuring the average electron trap density [Fig. 3(c)]. In the linear ohmic region, the estimated average electron trap density was 1.21 × 10^{9} cm^{-3} obtained by

$$n_{traps} = \frac{2\varepsilon\varepsilon_0 V_{TFL}}{eL^2}, \tag{3}$$

where ε and ε_0 denote the average dielectric constant (≈24) and vacuum permittivity, respectively, e is the elementary charge, and V_{TFL} is the voltage of the trap-filled limit.[30,31] This figure was nearly 30 times less than that of $MAPbBr_3$ PSCs (3.94 × 10^{10} cm^{-3}). Figure S5 illustrated the I–T curves of the device under 520 nm illumination under three different biases. The photoresponse of tin–lead HD was measured under different electric fields of −200, −300 , and −400 V cm^{-1} under 520 nm illumination with a power density of 2 mW cm^{-2}. The dark current is as low as 42, 86 and 115 nA, respectively, at three kinds of operating voltages. The sharp rise and decline curves without exponential decay also indicated few carriers trapping within the materials. Figure S6 illustrated that −400 V cm^{-1} was chosen as the operating electric field, which showed that the x-ray response current is close to saturation. Meanwhile, the x-ray detection capability of the tin–lead HD was characterized when the applied electric fields swept from −50 to −400 V cm^{-1} as shown in Fig. 3(d). The voltage of the x-ray tube is 40 kVp, and the tube current is 80 μA. From the picture, we can see that the device exhibited a significant and rapid response to x rays under different biases. The x-ray detection sensitivity was measured at 6.76 × 10^{4} μC Gy^{-1} cm^{-2} of the tin–lead HD and 6.8 × 10^{3} μC Gy^{-1} cm^{-2} of the $MAPbBr_3$ PSC under the electric field of −400 V cm^{-1} and tube voltage of 40 kVp [Fig. 3(e)]. We have achieved a nearly ten times higher x-ray detection sensitivity than before via improvements in materials and structure. Figure 3(f) shows the response to low-dose-rate x-ray photons under the electric field of −400 V cm^{-1}. The lowest detectable dose rate was 7.4 nGy s^{-1}. For harder x-ray photons, the x-ray detection sensitivities with 50, 80, and 120 kVp (which are widely used for medical measurement) were measured, as shown in

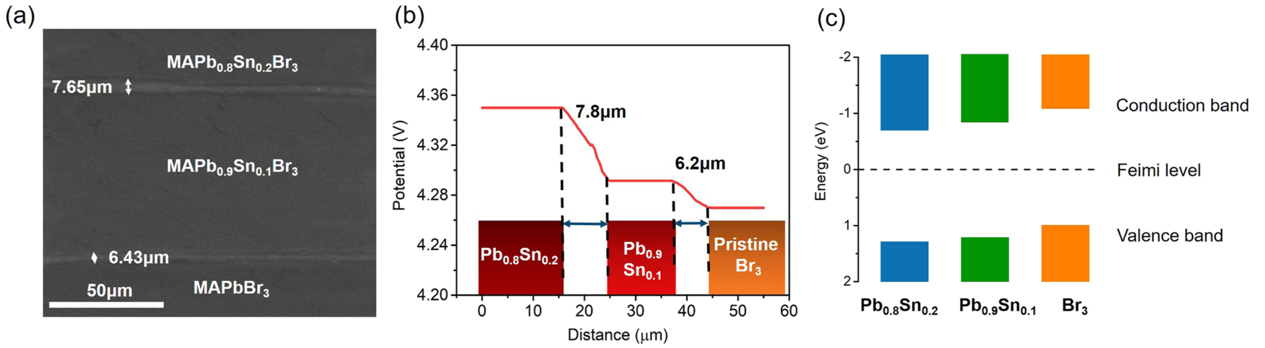

FIG. 2. The structure of tin–lead HD. (a) Depletion layer measured by SEM. (b) Width and energy barrier of heterojunction contact measured by KPFM. (c) Energetic levels of the $MAPbBr_3$, $MAPb_{0.9}Sn_{0.1}Br_3$, and $MAPb_{0.8}$ $Sn_{0.2}Br_3$ PSCs.

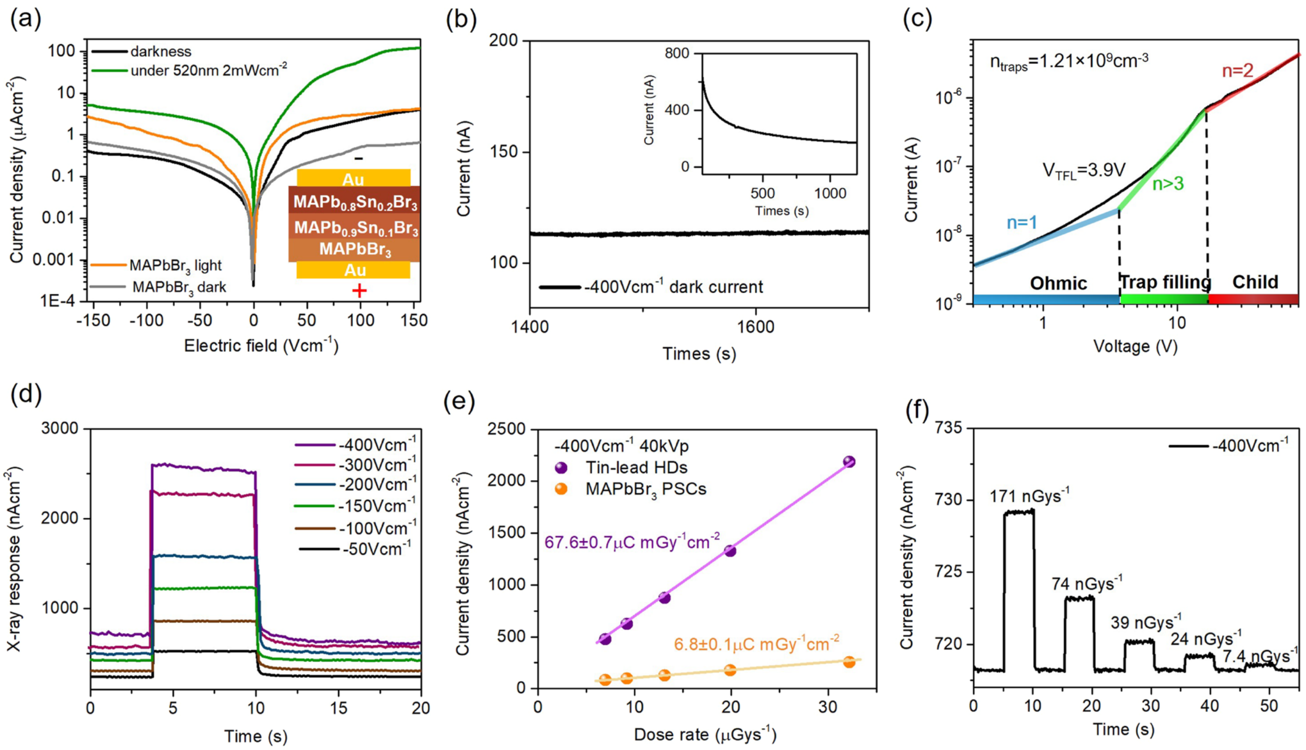

FIG. 3. Basic photoelectric characteristics and x ray detection performance. (a) I–V characterization of MAPbBr$_3$ PSC and tin–lead HD. (b) The dark current of the detector. The inset: Curve of dark current over time after applying voltage. (c) SCLC measurement for trap density. (d) Tin–lead HD response to x-ray pulses with varying applied bias voltage. (e) 40 kVp X-ray sensitivity of tin–lead HD and MAPbBr$_3$ PSC under −400 V cm^{-1} bias. (f) Current density with different low dose rate (40 kVp) under −400 V cm^{-1} electric field.

Fig. S7. The x-ray detection sensitivity decreases from 3.07×10^4 to 2.05×10^4 μC Gy^{-1} cm^{-2} and 7.8×10^3 μC Gy^{-1} cm^{-2}. Although the hard x-ray detection sensitivity has decreased to a certain extent, this figure is still similar to that of high-performance x-ray detectors (~7.1×10^3 μC Gy^{-1} cm^{-2}).[39]

In addition to the wide application of x rays in medical imaging, targeted radionuclide drugs have been proposed to carry out targeted tumor treatment by radiating α-particles recently. Hence, the detection of α-particles is of great significance. Here, we analyzed the device's response to α-particles and reported on the basic charge transport behaviors of tin–lead HD. The schematic illustration of alpha detection is shown in Fig. S8. High bias voltage needs to be applied to the detector to achieve higher charge collection efficiency. The process for testing the tin–lead HD is schematically described in Fig. 4(a). The drifting carriers will generate charge pulse signals in the preamplifier. Then, the output pulse from the preamplifier is processed by the shaping amplifier to form a pulse with a Gaussian shape. Finally, the multi-channel analyzer will measure the height of the Gaussian pulses to produce energy spectra.[32] The fully fabricated tin–lead HD and MAPbBr$_3$ PSC are shown in Fig. 4(b). When it comes to the α-particle response of two detectors under the same electric field intensity, tin–lead HD had more peaks and larger peak amplitudes compared to MAPbBr$_3$ within the same time range, demonstrating better α-particle detection capabilities. The number of electrons causing noise fluctuations was obtained by

$$noise = \frac{V}{Ce} electrons, \tag{4}$$

where C denotes the amplification coefficient of amplifier (≈1.4×10^{13} V/C), e is the elementary charge (≈1.6×10^{-19} C), and V is the voltage of fluctuation. The noise of tin–lead HDs (4.46×10^4 electrons) is apparently lower than that of MAPbBr$_3$ PSCs (1.48×10^5 electrons). The time-of-flight (TOF) method is used to evaluate the charge carrier mobility. We got the carrier drift time by calculating the pulse height rise time (the time required for the pulse to rise from 10% of the steady-state value to 90%). Figure 4(c) illustrates the typical transient pulses under different applied biases. The average electron rise time was estimated as 22.37 μs at 40 V, 16.16 μs at 80 V, 13.26 μs at 120 V, and 11.8 μs at 160 V. μ_e can be derived by the following equation:

$$\frac{1}{U} = \frac{\mu_e}{d^2} \times t_{drift}, \tag{5}$$

where d is the thickness of the detector (0.6 cm) and U is the applied bias. The carrier mobility can be examined by fitting the plot of 1/V–t. As shown in Fig. 4(d), the mobility of electrons in tin–lead HDs was estimated to be 612 cm^2 s^{-1} V^{-1}, which is nearly 30 times

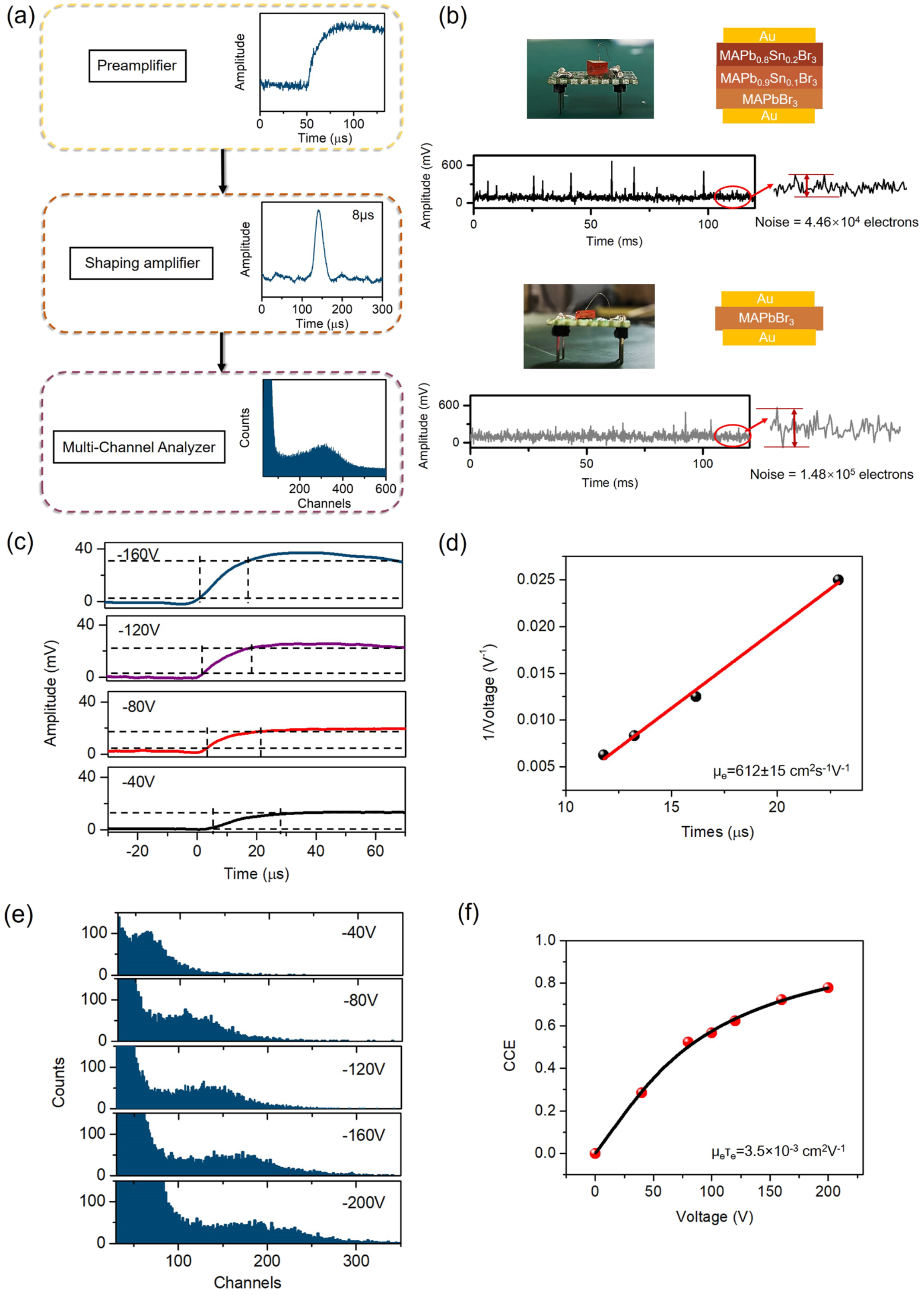

FIG. 4. α-particle radiation detection. (a) Diagram of the setup of α-particle response measurements. (b) Photographs of fabricated heterojunction detectors and $MAPbBr_3$ single crystals and their α-particle response and noise. (c) Typical α-particle induced output pulse shapes under various biases. (d) 1/V as a function of electron drift time. (e) α-spectra after applying various voltages to the heterojunction detector. (f) Mobility-lifetime product was fitting for the electron using the Hecht equation.

TABLE I. Summary on x-ray detection sensitivity, carrier mobility, and mobility-lifetime product tested by ^{241}Am (5.95 MeV) α particles of different perovskites.

Perovskites	X-ray sensitivity (μC Gy^{-1} cm^{-2})	μ_e (cm^2 s^{-1} V^{-1})	μ_h (cm^2 s^{-1} V^{-1})	$(\mu\tau)_e$ (cm^2 V^{-1})	$(\mu\tau)_h$ (cm^2 V^{-1})	References
$MAPbBr_3$ SC	6.8×10^3 (40 keV)	24.6	59.7	2.2×10^{-4}	4.2×10^{-4}	13 and 33
$MAPbI_3$ wafer	1.22×10^5 (40 keV)	70	48	7.4×10^{-4}	8.1×10^{-4}	34 and 35
$FAPbBr_3$ SC	–	22.2	66.1	8.0×10^{-4}	1.1×10^{-3}	36
$CsPbBr_3$ SC	1.25×10^3 (40 keV)	63	49	4.5×10^{-4}	9.5×10^{-4}	37 and 38
$FACsPbBr_3$ SC	–	189	262	1.8×10^{-3}	2.9×10^{-3}	11
Our detector	6.76×10^4 (40 keV)	612	–	3.5×10^{-3}	–	This work

large than that of $MAPbBr_3$ single crystals (~24.6 cm^2 s^{-1} V^{-1}). It is obvious that our device can promote mobility efficiently.

After applying high voltage, the electron–hole pairs generated by particles are separated and collected by two metal contacts, forming an energy spectrum. A series of the energy spectra of alpha particles were measured under various voltages applied for 30 s [Fig. 4(e)]. The peak centroids in the spectra moved to higher channels with increasing bias due to a higher charge collection efficiency (CCE). The single-carrier Hecht equation was used to estimate the mobility-lifetime product (μτ) based on the spectroscopy measurements,

$$\mathrm{CCE} = \frac{Q}{Q_0} = \frac{\mu\tau U}{d^2} \cdot \left(1 - e^{-\frac{d^2}{\mu\tau U}}\right), \tag{6}$$

where U is the applied bias, d is the thickness, Q is the measured peak channel number at applied bias V, and Q_0 is the calculated saturated channel number of the peak. It is shown in Fig. 4(f) that the corresponding data were fitted by the Hecht equation and the resulting value of $\mu_e\tau_e$ of 3.5×10^{-3} cm^2 V^{-1} was computed. Since μ_e is known, the electron lifetime can be estimated to be 5.72 μs. In Table I, we summarize the sensitivity of the x-ray detection and the carrier transport properties (mobility and μτ) of various hybrid halide perovskites. It is obvious that our detector has competitive x-ray detection performance and carrier transport properties.

We also designed the $MAPb_{0.8}Sn_{0.2}Br_3$–$MAPbBr_3$–$MAPb_{0.8}Sn_{0.2}Br_3$ (n–i–n) structure detector to compare the differences in performance between two types of structures [Figs. S9(a)–S9(e)]. The response of α-particles of the n–i–n structure detector is shown in Fig. S9(b). It is clear that the noise of this device is greater and the fluctuations are more pronounced under the same electric field intensity. Figure S9(c) describes the typical α-particle induced output pulses, and we can easily find that the response speed of the device has been significantly improved for 22.6 μs at 20 V, 11.2 μs at 80 V, 4.2 μs at 120 V, and 2.2 μs at 160 V, respectively. The mobility of electrons was derived as 405.7 cm^2 s^{-1} V^{-1}, which experiences a certain degree of decline. It can also be seen from the α-spectra [Fig. S9(e)] that the calculated saturated channel number of the peak of this n–i–n detector is much larger than that of the p–n structure detector, resulting in a significant decrease in the charge collection efficiency and carrier mobility-lifetime product.

CONCLUSION

In conclusion, we have confirmed that tin–lead PSCs have stronger stability compared to polycrystalline films. With tin ions, the single crystals change from p-type semiconductors to n-type. The carrier lifetimes and mobility of PSCs have been improved efficiently. Meanwhile, tin–lead gradient $MAPbBr_3$–$MAPb_{0.9}Sn_{0.1}Br_3$–$MAPb_{0.8}Sn_{0.2}Br_3$ heterojunction detectors were prepared for x-ray and α-particle pulse height spectra testing. The p–n structure can help the detector effectively suppress dark current. This detector also produces a good x-ray sensitivity of up to 6.76×10^4 μC Gy^{-1} cm^{-2}. The hole mobility is obtained as high as 612 cm^2 s^{-1} V^{-1} evaluated by the TOF technique. The mobility-lifetime (μτ) product for an electron is 3.5×10^{-3} cm^2 V^{-1} by fitting the corresponding pulse height spectra using the Hecht equation. We also find that the n–i–n structure detector has a faster response speed but a lower mobility-lifetime product. These results and insights will have a significant impact on the strategies to apply tin–lead alloy PSCs to the field of high-energy detection. Future efforts may focus on further improving the structure of the device, reducing the noise, and promoting the response of the tin–lead alloy PSCs detectors for good γ-ray detection.

EXPERIMENTAL SECTION

Materials

Lead bromide ($PbBr_2$, 99%), stannic bromide ($SnBr_2$), and methylammonium bromide (MABr) were purchased from Sigma-Aldrich, USA. Dimethylformamide-d7 (DMF) is obtained from Aladdin. Metallic gold, silver, and gadolinium were purchased from Chinese reagent, China.

Fabrication of $MAPbBr_3$, $MAPb_{0.9}Sn_{0.1}Br_3$ and $MAPb_{0.8}Sn_{0.2}Br_3$ PSCs

First, fully dissolve the MABr powder prepared in the previous step in DMF. When preparing the 1 mol/l $MAPbBr_3$ precursor, the 1 mol/l $PbBr_2$ powder needs to be weighed and stirred fully with a glass rod to dissolve it in the solution and filtered to obtain a clear $MAPbBr_3$ solution. When configuring 1 mol/l $MAPb_{0.9}Sn_{0.1}Br_3$ and 1 mol/l $MAPb_{0.8}Sn_{0.2}Br_3$ precursor, the molar ratios of $PbBr_2$ powder and $SnBr_2$ powder were 1:9(0.1 mol/l: 0.9 mol/l) and 2:8(0.2 mol/l: 0.8 mol/l), respectively, allowing them to fully dissolve.

In response to the low solubility of Sn^{2+} after addition, a beaker containing the solution can be added to a magnetic rotor and placed on a heating table for heating and stirring. After sufficient dissolution, clear $MAPb_{0.9}Sn_{0.1}Br_3$ and $MAPb_{0.8}Sn_{0.2}Br_3$ solutions can be obtained by filtration.

This study adopts the method of reverse temperature crystallization to grow $MAPbBr_3$, $MAPb_{0.9}Sn_{0.1}Br_3$ and $MAPb_{0.8}Sn_{0.2}Br_3$ PSCs. First, take about 40 ml of filtered MAPbBr3 precursor solution and pour it into a cleaned and dried crystallization dish. Place the crystallization dish on a heating table. Set the initial temperature of the heating table to 60 °C, raise the temperature by 1 °C every 5 h until 75 °C, and continue heating for several hours. The growth methods of the other two crystals are the same as above.

Fabrication of $MAPbBr_3$–$MAPb_{0.9}Sn_{0.1}Br_3$–$MAPb_{0.8}Sn_{0.2}Br_3$ structure detectors

First, place the $MAPbBr_3$ single crystal substrate into a clean and dried crystallization dish and pour about 30 ml of filtered and clarified $MAPb_{0.9}Sn_{0.1}Br_3$ precursor. Place the crystallization dish on a heating table without covering it. Set the temperature of the heating table to 68 °C to raise the temperature of the crystal and precursor together. If there is a temperature difference between the crystal and precursor, the surface of the substrate is likely to dissolve or crack. After about 30 min of evaporation after opening the lid, cover the lid and continue heating for 3–4 h to remove, obtaining $MAPbBr_3$ PSC wrapped in a layer of $MAPb_{0.9}Sn_{0.1}Br_3$ PSC. Next, place this crystal in a crystallization dish, pour about 30 ml of filtered clear $MAPb_{0.8}Sn_{0.2}Br_3$ precursor, repeat the above steps, and finally obtain a three-layer heterojunction structure of $MAPbBr_3$–$MAPb_{0.9}Sn_{0.1}Br_3$–$MAPb_{0.8}Sn_{0.2}Br_3$.

SUPPLEMENTARY MATERIAL

The supplementary material contains the whole XPS spectra of $MAPb_{0.9}Sn_{0.1}Br_3$ and $MAPb_{0.8}Sn_{0.2}Br_3$, photo of detectors, schematic of the KPFM measurement, and data of α-particle radiation detection of the n-i-n structure (PDF).

ACKNOWLEDGMENTS

This work was financially supported by the National Key Research and Development Program of China (Grant Nos. 2021YFE0105900 and 2022YFE0139100), the National Natural Science Foundation Project of China (Grant Nos. 62175028, 51879042, 61674029, and 12375306), the National Natural Science Foundation Project for Young Researcher (Grant No. 12005038), Program 111_2.0 in China (Grant No. BP0719013), the Leading Technology of Jiangsu Basic Research Plan (Grant No. BK20192003), and the International cooperative research project of Jiangsu province (Grant No. BZ2022008).

AUTHOR DECLARATIONS

Conflict of Interest

The authors have no conflicts to disclose.

Author Contributions

J.W., X.W., Y.X., and Y.P. contributed to the fabrication of the heterojunction detectors, and J.W., S.C., and Q.C. contributed to grow perovskite single crystals. J.W. and J.Z. conducted x-ray detection. J.W., X.W., and Y.X. took the α-particle detection experiment. J.W. wrote this manuscript. All authors helped revise the manuscript.

Jie Wu: Conceptualization (equal); Data curation (equal); Formal analysis (equal); Funding acquisition (equal); Investigation (equal); Methodology (equal); Project administration (equal); Resources (equal); Software (equal); Supervision (equal); Validation (equal); Visualization (equal); Writing – original draft (equal); Writing – review & editing (equal). **Xin Wang**: Conceptualization (equal); Data curation (equal); Formal analysis (equal); Methodology (equal); Resources (equal). **Yubing Xu**: Conceptualization (equal); Data curation (equal); Methodology (equal); Resources (equal). **Yuzhu Pan**: Conceptualization (equal); Methodology (equal); Resources (equal). **Shunjie Chai**: Data curation (equal); Methodology (equal). **Jingda Zhao**: Methodology (equal); Resources (equal). **Qi Cheng**: Resources (equal). **Zhiwei Zhao**: Methodology (equal). **Qing Li**: Methodology (equal). **Byung Seong Bae**: Methodology (equal). **Omolola Esther Fayemi**: Methodology (equal). **Jianming1 Zhou**: Methodology (equal). **Ying Zhu**: Methodology (equal). **Wei Lei**: Methodology (equal); Resources (equal); Writing – review & editing (equal).

DATA AVAILABILITY

The data that support the findings of this study are available from the corresponding authors upon reasonable request.

REFERENCES

[1] D. Mery and D. Filbert, "Automated flaw detection in aluminum castings based on the tracking of potential defects in a radioscopic image sequence," IEEE Trans. Robot. Autom. **18**, 890–901 (2002).

[2] F. Arfelli, M. Assante, V. Bonvicini, A. Bravin, G. Cantatore, E. Castelli, L. D. Palma, M. D. Michiel, R. Longo, A. Olivo, S. Pani, D. Pontoni, P. Poropat, M. Prest, A. Rashevsky, G. Tromba, A. Vacchi, E. Vallazza, and F. Zanconati, "Low-dose phase contrast x-ray medical imaging," Phys. Med. Biol. **43**, 2845 (1998).

[3] P. Bijl, M. A. Hogervorst, J. M. Valeton *et al.*, BAXSTER: An image quality tester for X-ray baggage screening systems, *Sensors, and Command, Control, Communications, and Intelligence (C3I) Technologies for Homeland Defense and Law Enforcement. II* (International Society for Optics and Photonics, 2003), pp. 341–351.

[4] C. C. Stoumpos, C. D. Malliakas, J. A. Peters, Z. Liu, M. Sebastian, J. Im, T. C. Chasapis, A. C. Wibowo, D. Y. Chung, A. J. Freeman, B. W. Wessels, and M. G. Kanatzidis, "Crystal growth of the perovskite semiconductor $CsPbBr_3$: A new material for high-energy radiation detection," Cryst. Growth Des. **13**, 2722–2727 (2013).

[5] S. Yakunin, M. Sytnyk, D. Kriegner, S. Shrestha, M. Richter, G. J. Matt, H. Azimi, C. J. Brabec, J. Stangl, M. V. Kovalenko, and W. Heiss, "Detection of X-ray photons by solution-processed lead halide perovskites," Nat. Photonics **9**, 444–449 (2015).

[6] T. Zuo, X. He, P. Hu, and H. Jiang, "Organic-inorganic hybrid perovskite single crystals: Crystallization, molecular structures, and bandgap engineering," CHEMNANOMAT **5**, 278–289 (2019).

[7] Y. Kim, K. Kim, DY. Son, D. N. Jeong, J. Y. Seo, Y. S. Choi, I. T. Han, S. Y. Lee, and N. G. Park, "Printable organometallic perovskite enables large-area, low-dose X-ray imaging," Nature **550**, 87–91 (2017).

[8] G. Wang, M. Amman, H. Mei, D. Mei, K. Irmscher, Y. Guan, and G. Yang, “Crystal growth and detector performance of large size High-purity Ge crystals,” Mater. Sci. Semicond. Process. **39**, 54–60 (2015).

[9] F. Zhang, C. Herman, Z. He, G. De Geronimo, E. Vernon, and J. Fried, “Characterization of the H3D ASIC readout system and 6.0 cm^3 3-D position sensitive CdZnTe detectors,” IEEE Trans. Nucl. Sci. **59**, 236–242 (2012).

[10] S. Yakunin, D. Dirin, Y. Shynkarenko, V. Morad, I. Cherniukh, O. Nazarenko, D. Kreil, T. Nauser, and M. V. Kovalenko, “Detection of gamma photons using solution-grown single crystals of hybrid lead halide perovskites,” Nat. Photonics **10**, 585–589 (2016).

[11] L. Zhao, Y. Zhou, Z. Shi, Z. Ni, M. Wang, Y. Liu, and J. Huang, “High-yield growth of $\mathrm{FACsPbBr_3}$ single crystals with low defect density from mixed solvents for gamma-ray spectroscopy,” Nat. Photonics **17**, 315–323 (2023).

[12] Y. He, M. Petryk, Z. Liu, D. G. Chica, I. Hadar, C. Leak, W. Ke, I. Spanopoulos, W. Lin, D. Y. Chung, B. W. Wessels, Z. He, and M. G. Kanatzidis, “$\mathrm{CsPbBr_3}$ perovskite detectors with 1.4% energy resolution for high-energy γ-rays,” Nat. Photonics **15**, 36–42 (2021).

[13] X. Liu, H. Zhang, B. Zhang, J. Dong, W. Jie, and Y. Xu, “Charge transport behavior in solution-grown methylammonium lead tribromide perovskite single crystal using α particles,” J. Phys. Chem. C **122**, 14355–14361 (2018).

[14] Q. Xu, H. Wei, W. Wei, W. Chuirazzi, D. DeSantis, J. Huang, and L. Cao, “Detection of charged particles with a methylammonium lead tribromide perovskite single crystal,” Nucl. Instrum. Methods Phys. Res., Sect. A **848**, 106–108 (2017).

[15] E. Lukosi, T. Smith, J. Tisdale, D. Hamm, C. Seal, B. Hu, and M. Ahmadi, “Methylammonium lead tribromide semiconductors: Ionizing radiation detection and electronic properties,” Nucl. Instrum. Methods Phys. Res., Sect. A **927**, 401–406 (2019).

[16] L. Kong, G. Liu, J. Gong, Q. Hu, R. D. Schaller, P. Dera, D. Zhang, Z. Liu, W. Yang, K. Zhu, Y. Tang, C. Wang, S. H. Wei, T. Xu, and H. k. Mao, “Simultaneous band-gap narrowing and carrier-lifetime prolongation of organic–inorganic trihalide perovskites,” Proc. Natl. Acad. Sci. U. S. A. **113**, 8910 (2016).

[17] G. Xiao, Y. Cao, G. Qi, L. Wang, C. Liu, Z. Ma, X. Yang, Y. Sui, W. Zheng, and B. Zou, “Pressure effects on structure and optical properties in cesium lead bromide perovskite nanocrystals,” J. Am. Chem. Soc. **139**, 10087 (2017).

[18] S. Gu, R. Lin, Q. Han, Y. Gao, H. Tan, and J. Zhu, “Tin and mixed lead–tin halide perovskite solar cells: Progress and their application in tandem solar cells,” Adv. Mater. **32**, 1907392 (2020).

[19] H. Yao, F. Zhou, Z. Li, Z. Ci, L. Ding, and Z. Jin, “Strategies for improving the stability of tin-based perovskite ($\mathrm{ASnX_3}$) solar cells,” Adv. Sci. **7**, 1903540 (2020).

[20] F. Hao, C. C. Stoumpos, R. Chang, and M. G. Kanatzidis, “Anomalous band gap behavior in mixed Sn and Pb perovskites enables broadening of absorption spectrum in solar cells,” J. Am. Chem. Soc. **136**, 8094–8099 (2014).

[21] F. Zuo, S. T. Williams, P.-W. Liang, C. C. Chueh, C. Y. Liao, and A. K. Y. Jen, “Binary-metal perovskites toward high-performance planar-heterojunction hybrid solar cells,” Adv. Mater. **26**, 6454–6460 (2014).

[22] C. C. Stoumpos, C. D. Malliakas, and M. G. Kanatzidis, “Semiconducting tin and lead iodide perovskites with organic cations: Phase transitions, high mobilities, and near-infrared photoluminescent properties,” Inorg. Chem. **52**, 9019–9038 (2013).

[23] Y. Lei, Y. Chen, R. Zhang, Y. Li, Q. Yan, S. Lee, Y. Yu, H. Tsai, W. Choi, K. Wang, Y. Luo, Y. Gu, X. Zheng, C. Wang, C. Wang, H. Hu, Y. Li, B. Qi, M. Lin, Z. Zhang, S. A. Dayeh, M. Pharr, D. P. Fenning, Y. H. Lo, J. Luo, K. Yang, J. Yoo, W. Nie, and S. Xu, “A fabrication process for flexible single-crystal perovskite devices,” Nature **583**, 790–795 (2020).

[24] M. Xiao, S. Gu, P. Zhu, M. Tang, W. Zhu, R. Lin, C. Chen, W. Xu, T. Yu, and J. Zhu, “Tin-based perovskite with improved coverage and crystallinity through tin-fluoride-assisted heterogeneous nucleation,” Adv. Opt. Mater. **6**, 1700615 (2018).

[25] X. Xu, C. C. Chueh, Z. Yang, A. Rajagopal, J. Xu, S. B. Jo, and A. K. Y. Jen, “Ascorbic acid as an effective antioxidant additive to enhance the efficiency and stability of Pb/Sn-based binary perovskite solar cells,” Nano Energy **34**, 392–398 (2017).

[26] Z. Yang, X. Zhang, W. Yang, G. E. Eperon, and D. S. Ginger, “Tin–lead alloying for efficient and stable all-inorganic perovskite solar cells,” Chem. Mater. **32**, 2782–2794 (2020).

[27] Y. Pan, X. Wang, Y. Liao, Y. Xu, Y. Li, Q. Li, X. Zhang, J. Chen, Z. Zhu, Z. Zhao, E. E. Elemike, M. Furuta, and W. Lei, “Epitaxial perovskite single-crystalline heterojunctions for filter-free ultra-narrowband detection with tunable spectral responses,” ACS Appl. Mater. Interfaces **14**, 50331–50342 (2022).

[28] P. Cui, D. Wei, J. Ji, H. Huang, E. Jia, S. Dou, T. Wang, W. Wang, and M. Li, “Planar p–n homojunction perovskite solar cells with efficiency exceeding 21.3%,” Nat. Energy **4**, 150–159 (2019).

[29] X. Wang, Y. Pan, Y. Xu, J. Zhao, Y. Li, Q. Li, J. Chen, Z. Zhao, X. Zhang, E. E. Elemike, D. C. Onwudiwe, B. S. Bae, and W. Lei, “High spectral-rejection-ratio narrowband photodetectors based on perovskite heterojunctions,” Adv. Electron. Mater. **8**, 2200178 (2022).

[30] J. Kim, J. Kwon, M. Kim, J. Do, D. Lee, and H. Han, “Low-dielectric-constant polyimide aerogel composite films with low water uptake,” Polym. J. **48**, 829–834 (2016).

[31] Y. Yuan and J. Huang, “Ion migration in organometal trihalide perovskite and its impact on photovoltaic efficiency and stability,” Acc. Chem. Res. **49**, 286–293 (2016).

[32] B.-B. Zhang, F. Wang, X. Liu, B. Xiao, M. Xu, S. T. Dong, Y. Xu, P. Sellin, and W. Jie, “Ion migration controlled stability in α-particle response of $\mathrm{CsPbBr_{2.4}Cl_{0.6}}$ detectors,” J. Phys. Chem. C **125**, 4235–4242 (2021).

[33] W. Wei, Y. Zhang, Q. Xu, H. Wei, Y. Fang, Q. Wang, Y. Deng, T. Li, A. Gruverman, L. Cao, and J. Huang, “Monolithic integration of hybrid perovskite single crystals with heterogenous substrate for highly sensitive X-ray imaging,” Nat. Photonics **11**, 315–321 (2017).

[34] M. Hu, S. Jia, Y. Liu, J. Cui, Y. Zhang, H. Su, S. Cao, L. Mo, D. Chu, G. Zhao, K. Zhao, Z. Yang, and S. F. Liu, “Large and dense organic–inorganic hybrid perovskite $\mathrm{CH_3NH_3PbI_3}$ wafer fabricated by one-step reactive direct wafer production with high X-ray sensitivity,” ACS Appl. Mater. Interfaces **12**, 16592–16600 (2020).

[35] Y. He, W. Ke, G. C. Alexander, K. M. McCall, D. G. Chica, Z. Liu, I. Hadar, C. C. Stoumpos, B. W. Wessels, and M. G. Kanatzidis, “Resolving the energy of γ-ray photons with $\mathrm{MAPbI_3}$ single crystals,” ACS Photonics **5**, 4132–4138 (2018).

[36] X. Liu, M. Xu, Y. Hao, J. Fu, F. Wang, B. Zhang, S. Bennett, P. Sellin, W. Jie, and Y. Xu, “Solution-grown formamidinium hybrid perovskite ($\mathrm{FAPbBr_3}$) single crystals for α-particle and γ-ray detection at room temperature,” ACS Appl. Mater. Interfaces **13**, 15383–15390 (2021).

[37] Y. He, Z. Liu, K. M. McCall, W. Lin, D. Y. Chung, B. W. Wessels, and M. G. Kanatzidis, “Perovskite $\mathrm{CsPbBr_3}$ single crystal detector for alpha-particle spectroscopy,” Nucl. Instrum. Methods Phys. Res., Sect. A **922**, 217–221 (2019).

[38] H. Zhang, F. Wang, Y. Lu, Q. Sun, Y. Xu, B.-B. Zhang, W. Jie, and M. G. Kanatzidis, “High-sensitivity X-ray detectors based on solution-grown caesium lead bromide single crystals,” J. Mater. Chem. C **8**, 1248–1256 (2020).

[39] X. Wang, Y. Xu, Y. Pan, Y. Li, J. Xu, J. Chen, J. Wu, Q. Li, X. Zhang, Z. Zhao, C. Li, E. E. Elemike, D. C. Onwudiwe, J. Akram, and W. Lei, “Low-noise X-ray PIN photodiodes made of perovskite single crystals by solution-processed dopant incorporated epitaxial growth,” Nano Energy **89**, 106311 (2021).